A Single-Switch WPT Circuit With Inherent CCO–CVO for Battery Charging

Jingyu Wang, *Student Member, IEEE*, and Zhicong Huang, *Member, IEEE*

***Abstract*— In order to obtain a highly reliable and low-cost wireless charging method, this article proposes a single-switch wireless power transfer (WPT) circuit with inherent constant-current output (CCO) and constant-voltage output (CVO) for battery charging. Compared with a full-bridge WPT circuit, the structure and control strategy of the proposed circuit are simple. And the shoot-through problem could be avoided in the proposed circuit. In order to realize the inherent CCO–CVO without the wireless communication and extra control circuit, the double-D quadrature (DDQ) coils are used in this article to remove cross-coupling between coils. And the corresponding compensation network is designed to realize the automatic transition from the CCO to CVO. There are no active control schemes used in the proposed method. The compensation design could enable primary-side protection of over current against the accidental removal of the secondary side. There is no compensation inductor in the secondary circuit, which reduces the volume and weight of the secondary circuit. Moreover, the transfer gain does not rely on the transformer parameters, and more parameters design freedom can be realized. Finally, the simulation and the experimental verification are carried out to verify the superiority of the proposed circuit.**

***Index Terms*— Constant-current output (CCO), constant-voltage output (CVO), highly reliable, single switch, wireless power transfer (WPT).**

I. Introduction

WIRELESS power transfer (WPT) is known to be a convenient and safe way of charging or power supply since there being no physical connection between the primary and secondary circuits. It has been widely used in many systems and products with power levels ranging from low power to high power such as the battery charging of cell phones [1], [2], [3], LED driving [4], biomedical implants powering [5], [6], [7], [8], and electric vehicle (EV) charging [9], [10], [11], [12]. With the development of artificial intelligence, wireless charging technology has become indispensable. In order to extend the life span of the battery and ensure the safety of the charging process, the charging process is shown in Fig. 1; the initial constant-current output (CCO) charging mode and subsequent constant-voltage output (CVO) charging mode are necessary.

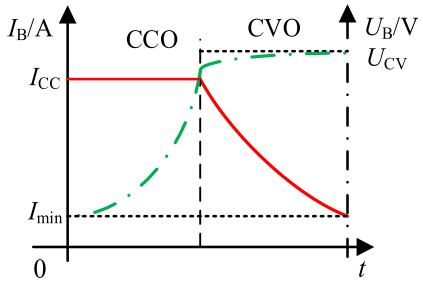

Fig. 1. Constant current and constant voltage charging curves of a lithium-ion battery.

In order to realize CCO and CVO in wireless charging systems, some effective methods have been proposed. Adding an additional dc–dc converter in the secondary circuit [13], [14] is an intuitive idea that could realize this target. However, the extra cost and power loss will be increased. Keeping a single-stage design in mind, the compensation network is studied to realize load-independent CCO or CVO. However, one kind of compensation network could only realize one single characteristic (CCO or CVO) at one frequency [15], [16]. Therefore, the hybrid topologies are studied to realize the switching between CCO and CVO by changing the structure of the compensation network [17], [18], [19], but the voltage stress on the mode switches is very high, and the extra switches reduce the reliability of the system. Therefore, some topologies with different characteristics (CCO and CVO) under different frequencies are proposed [20], [21], [22], and the switching from CCO to CVO charging modes can be realized by switching the operating frequency from f_{CC} to f_{CV}. In addition, although the above methods could realize both CCO and CVO in a single-stage design, battery state-of-charge (SOC) detection and wireless feedback communication are inevitable to ensure charging safety. However, the complex wireless communication and control circuits will also reduce the reliability of the system.

In order to realize inherent CCO to CVO transition capability, a novel clamp coil-assisted WPT battery charger is studied in [23], and the automatic transition from the CCO to the CVO could be achieved by the working of the clamp coil. In CCO mode, the circuit operates as a conventional series–series (SS) compensated WPT converter. And when the equivalent load of the battery is large enough, there will be current in the clamp coil, the input current of the primary

Manuscript received 22 November 2022; revised 21 February 2023; accepted 19 April 2023. Date of publication 28 April 2023; date of current version 16 March 2024. This work was supported in part by the National Natural Science Foundation of China under Grant 52007067 and in part by the Natural Science Foundation of Guangdong Province under Grant 2022A1515011581 and Grant 2023A1515011623. *(Corresponding author: Zhicong Huang.)*

The authors are with the Shien-Ming Wu School of Intelligent Engineering, South China University of Technology, Guangzhou 510006, China (e-mail: 202210190813@mail.scut.edu.cn; zhiconghuang@scut.edu.cn).

Digital Object Identifier 10.1109/TTE.2023.3271364

TABLE I
COMPARISON OF DIFFERENT SCHEMES FOR CCO–CVO

Type	CCO and CVO Method	Citations	Switches	Auxiliary driving circuit	Shoot-through problem	Active Control	Protection against removal of receiver	Inductors in the secondary circuit	Voltage stress of switches
Full-bridge	Inherent	[24]	4	complex	Yes	No	No	1	U_{DC}
	Frequency switching	[20]	4	complex	Yes	Yes	Only CCO mode	1	U_{DC}
	Hybrid	[18]	4	complex	Yes	Yes	Yes	1	U_{DC}
	DC-DC converter	[28]	5	complex	Yes	Yes	No	1	U_{DC}
Single-switch	Frequency switching	[26]	1	Simple	No	Yes	No	2	3~4U_{DC}
	Hybrid	[9]	1	Simple	No	Yes	No	1	3~4U_{DC}
	Inherent	Proposed	1	Simple	No	No	Yes	0	3~4U_{DC}

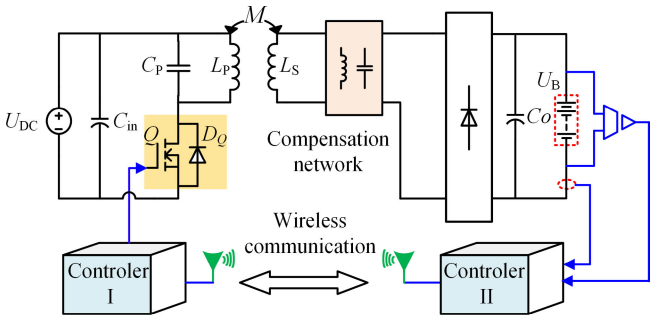

Fig. 2. Single-switch WPT system used for battery charging.

coil will be constant, and the circuit operates in CVO mode. In addition, a hybrid WPT system with inherent CCO–CVO characteristics is also studied to use in charging applications [24]. There are two primary coils and two secondary coils in this method, and the automatic transition from the CCO to the CVO could be achieved by blocking one of the secondary coils automatically when the equivalent load of the battery is large enough. According to the aforementioned methods, SOC detection and wireless feedback could be saved. However, the above methods are studied based on the full-bridge WPT circuit. Four switches and corresponding drive circuits are used in the circuit. And the coordination of four switches and the isolation of different drive signals should be considered. In addition, the above methods with the inherent CCO to CVO transition capability are based on the basic compensation network such as the SS compensation network, the transfer gain of the circuit relies on the transformer parameters, and the design freedom of a loosely coupled transformer (LCT) is limited.

Single-switch WPT circuit has only one switch, which reduces the switching loss, simplifies the control strategy, and does not have the risk of the shoot-through problem. Compared with full-bridge WPT circuits, single-switch circuits have more advantages in low-power occasions due to their low cost and high reliability. The single-switch WPT system used for battery charging is shown in Fig. 2. At present, the load-independent CCO and CVO have been studied in [25], [26], and [27]. The hybrid compensation network used in a single-switch WPT circuit has been studied in [25] to realize CCO and CVO, the circuit operates at a single operating frequency, and the extra switches are used to realize the switching between the P-S and P-CLC compensation networks. In addition to the hybrid topology, P-CLCL and P-CLC compensation networks are studied to realize CCO and CVO at two different operating frequencies without extra mode switches [26], [27]. Although the single-switch WPT circuit has higher reliability compared with the full-bridge WPT circuit, the transition from the CCO mode to the CVO mode in the above single-switch circuits still relies on the wireless communication or extra control circuit, which reduces the reliability of the charging system. The operation of a single-switch WPT circuit relies on the resonance between the capacitor in the primary circuit and part of the inductance of the primary coil. It makes the inherent CCO to CVO transition capability discussed in [23] and [24] very hard to realize in the single-switch WPT circuit. In order to further improve the reliability of the single-switch WPT circuit with CCO and CVO and obtain a kind of low-cost and highly reliable wireless charging method, consequently, research on the single-switch WPT circuit with inherent CCO–CVO output is necessary.

Although some schemes have been carried out to realize CCO and CVO for battery charging, as shown in Table I, there are still deficiencies which are summarized as follows.

1) There are at least four switches and auxiliary driving circuits used in the full-bridge circuit, which results in high costs. Moreover, the shoot-through problem cannot be avoided.
2) Existing single-switch WPT converters require wireless communication and SOC detection to realize CCO and CVO, which is an active control scheme and makes the system less rugged.
3) In [24], we have also pointed out its deficiencies in the introduction. Its compensation design cannot enable primary-side protection of over current against the accidental removal of the secondary and does not allow minimal compensation components in the secondary (which means the secondary will be clumsier). Moreover, since it is driven by a full-bridge inverter, it also suffers from the deficiencies mentioned in (1).

A single-switch WPT circuit with inherent CCO–CVO is proposed in this article as shown in Fig. 3 for battery charging. Different from the traditional single-switch WPT circuit

as shown in Fig. 2, an extra *LC* compensation network is added to the circuit to realize *LC* resonance and generate a high-frequency voltage source. The equivalent analysis of this kind of novel structure is operated in this article, and the fundamental component of the output of the inverter could be obtained. The double-D quadrature (DDQ) coils are used in this article to remove cross-coupling between coils. And the corresponding compensation network is designed to realize the automatic transition from CCO to CVO. The *LCL* compensation network in the primary circuit is used to obtain a CCO of the single-switch inverter. It creates conditions for the realization of an automatic transition from the CCO to the CVO. The compensation design could enable primary-side protection of over current against the accidental removal of the secondary side. And the proposed method allows minimal compensation components on the secondary side; there is no inductor in the secondary circuit. In addition, the transfer gain of the proposed circuit does not rely on the transformer parameters, which improves the design freedom of an LCT. Finally, a prototype of the single-switch WPT charger with 6-A charging current and 72-V battery voltage is built to verify the correction of analysis in this article.

To this end, the contributions of this article are shown as follows.

1) A fully passive single-switch driven WPT converter with inherent CCO–CVO capability is proposed, which features the elimination of wireless communication, ease of control, rugged, and no shoot-through problem.
2) The compensation design could enable primary-side protection of over current against the accidental removal of the secondary side.
3) Only capacitors compensation design in the secondary circuit, which reduces the volume and weight of the secondary circuit.

The rest of this article is organized as follows. The analysis of the single-switch *LC*-resonant circuit and the calculated method of the output voltage of the inverter is detailed in Section II. The principle of the inherent CCO and CVO in the proposed single-switch WPT circuit is analyzed in Section III. And the characteristics of the proposed circuit and the design of parameters are discussed in Section IV. The performance of the proposed circuit is evaluated in Section V. Section VI concludes this article.

II. Analysis of Single-Switch LC-Resonant Circuit

Fig. 3 shows the proposed single-switch WPT circuit with the inherent CCO–CVO output. The circuit on the primary side includes a single-switch *LC*-resonant inverter and two compensation networks in parallel. Q is the MOSFET in the single-switch *LC*-resonant circuit. And the extra L_x and C_p are used to compose the *LC*-resonant circuit. C_1, C_2, C_3, and C_4 are compensated capacitors. And L_1 and L_2 are the compensated inductors. The LCT consists of two groups of coils. L_{p1} and L_{s1} are double-D (DD) coils, and L_{p2} and L_{s2} are unipolar coils. M_{12} and M_{34} are their mutual inductance, respectively. C_5 and C_6 are the compensated capacitors on the secondary side. And the outputs of two rectifier bridges are connected in parallel, and every rectifier bridge is composed of four diodes.

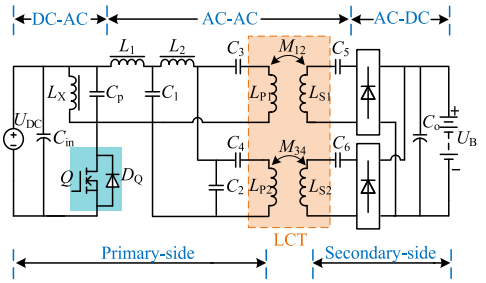

Fig. 3. Proposed single-switch circuit with inherent CCO–CVO output.

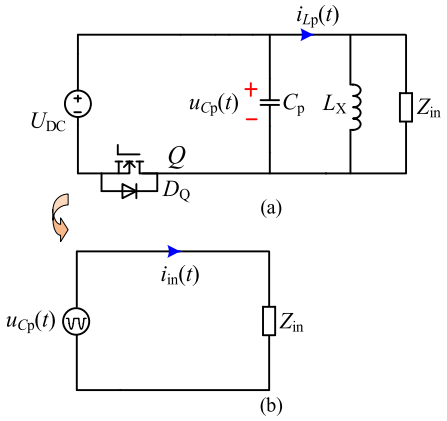

Fig. 4. Equivalent circuit of the proposed circuit: (a) equivalent circuit and (b) simplified equivalent circuit.

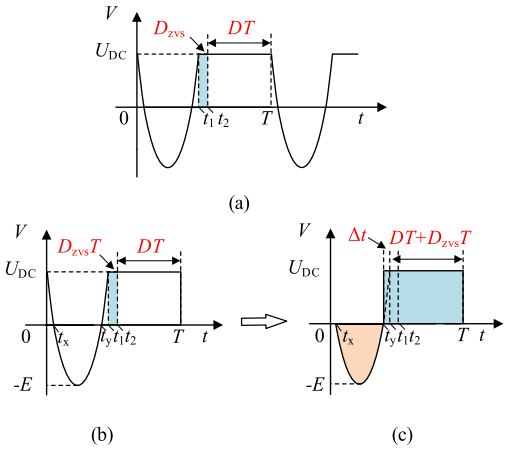

Fig. 5. Waveforms of $u_{Cp}(t)$: (a) waveform of $u_{Cp}(t)$; (b) waveform of $u_{Cp}(t)$ in one operating period; and (c) simplified waveform of $u_{Cp}(t)$ in one operating period.

The equivalent circuit of the inverter in Fig. 3 is shown in Fig. 4, which is different from the traditional single-switch WPT circuit. Due to the extra *LC* compensation network, Fig. 4(b) could be obtained from Fig. 4(a), the input voltage does not rely on the primary coil like the traditional single-switch WPT circuit, and the independent source could be realized. The output voltage of the single-switch inverter is $u_{Cp}(t)$, which is shown in Fig. 5(a). When the MOSFET Q or the antiparallel diode D_Q is turned on, the voltage of C_p

is U_{dc}. When the MOSFET works at the blocking state, the voltage waveform of C_p is an underdamped waveform.

When the MOSFET is turned off and before the antiparallel diode is turned on, the state equation of the circuit could be expressed as follows:

$$\begin{cases} L_X \dfrac{di_{Lx}(t)}{dt} = u_{Cp}(t) \\ i_{Lx}(t) + C_p \dfrac{du_{C_p}(t)}{dt} + \dfrac{u_{C_p}(t)}{Z_{in}} = 0 \end{cases} \tag{1}$$

where Z_{in} is the input impedance.

Then, $u_{Cp}(t)$ could be expressed by the following equation:

$$u_{C_p}(t) = -Ee^{\alpha t}\sin(\omega' t + \varphi) \tag{2}$$

where

$$\begin{cases} \alpha = -\dfrac{1}{2C_p Z_{in}} \\ \omega' = \sqrt{\dfrac{4Z_{in}^2 C_p - L_X}{4C_p^2 L_X Z_{in}^2}}. \end{cases} \tag{3}$$

Therefore, as shown in Fig. 5(a), the expression of $u_{Cp}(t)$ in one switching period T could be expressed by the following equation:

$$u_{C_p}(t) = \begin{cases} -Ee^{\alpha t}\sin(\omega' t + \varphi) & (0 < t < t_1) \\ U_{DC} & (t_1 \le t \le T). \end{cases} \tag{4}$$

In this article, the operational angular frequency $\omega = 2\pi/T$, $t_1 < T/2$, and set $\omega_1 = 2\pi/t_1$ and then $\omega_1 > 2\omega$. The following equation should be satisfied:

$$e^{\alpha \frac{1}{2\omega}} < e^{\alpha t} \le 1. \tag{5}$$

In general, the value of $1/(4\omega_s C_p Z_{in})$ is very low, and the value of e^{at} could be regarded as 1. Then, the expression of $u_{Cp}(t)$ in (4) could be expressed by the following equation:

$$u_{C_p}(t) = \begin{cases} -E\sin(\omega' t + \varphi) & (0 < t < t_1) \\ U_{DC} & (t_1 \le t \le T) \end{cases} \tag{6}$$

where E is the amplitude of the sinusoidal wave in Fig. 5(b) and φ is its phase angle.

To facilitate calculation, the waveform of $u_{Cp}(t)$ could be approximated as Fig. 5(c) from Fig. 5(b). The value of ω' and φ could be expressed by the following equation as shown in Fig. 5(c):

$$\begin{cases} \omega' = \dfrac{\pi}{t_y - t_x} = \dfrac{\pi}{(1 - D - D_{ZVS})T - 2\Delta t} \\ \varphi = \dfrac{-2\pi t_x}{T} \end{cases} \tag{7}$$

where D is the duty cycle of MOSFET and D_{ZVS} is the zero-voltage switching (ZVS) margin of the MOSFET; according to $u_{Cp}(0) = U_{dc}$, the Δt could be expressed by

$$\Delta t = t_x - 0 = t_1 - t_y = \frac{\pi \cdot \arcsin\left(\frac{U_{DC}}{E}\right)}{180^\circ \cdot \omega'}. \tag{8}$$

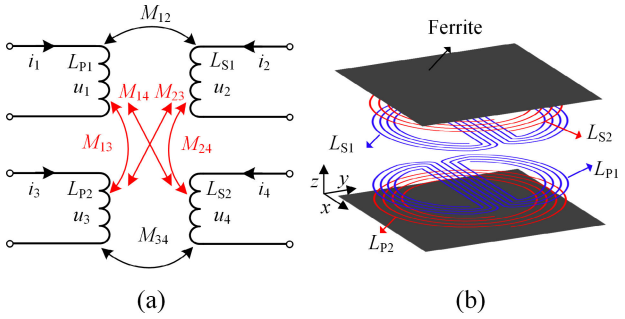

Fig. 6. Model of the LCT: (a) cross-coupling among coils and (b) structure of the DDQ coils.

As shown in Fig. 5(c), the balance of the volt-second product of C_p should be satisfied in one switching, which could be expressed by the following equation:

$$\begin{aligned} U_{DC} \cdot (T - t_y) &= \left(\frac{1}{t_y - t_x}\int_{t_x}^{t_y} E\sin(\omega' t)dt\right)(t_y - t_x) \\ &= \frac{2E}{\pi}(t_y - t_x). \end{aligned} \tag{9}$$

Therefore, the value of E could be calculated by the following equation:

$$E = \frac{\pi U_{DC} \cdot [(D + D_{ZVS})T + \Delta t]}{2[(1 - D - D_{ZVS})T - 2\Delta t]}. \tag{10}$$

As shown in (10), when the input voltage U_{dc}, D, D_{ZVS}, and operating frequency are determined, the value of E could be calculated by (7), (8), and (10). In this article, U_{dc} is 96 V, and D and D_{ZVS} are 0.55 and 0.08, respectively. And the operating frequency is 85 kHz. The E could be calculated as 332.4 V. The voltage stress of the MOSFET is equal to $E+ U_{dc}$, which could be calculated as 428.4 V.

The Fourier decomposition of the curve in Fig. 5(c) could be expressed by the following equation:

$$\begin{cases} a_1 = \dfrac{2}{T}\displaystyle\int_{t_x}^{t_y}(-E)\sin(\omega' t)\sin(\omega_o t)dt \\ \qquad + \dfrac{2}{T}\displaystyle\int_{t_y}^{T} U_{DC}\sin(\omega_o t)dt \\ b_1 = \dfrac{2}{T}\displaystyle\int_{t_x}^{t_y}(-E)\sin(\omega' t)\cos(\omega_o t)dt \\ \qquad + \dfrac{2}{T}\displaystyle\int_{t_y}^{T} U_{DC}\cos(\omega_o t)dt. \end{cases} \tag{11}$$

Therefore, the amplitude of the fundamental component of $u_{Cp}(t)$ could be expressed by the following equation:

$$A_1 = \sqrt{a_1^2 + b_1^2}. \tag{12}$$

III. Principle of the Realization of Inherent CCO and CVO in the Proposed Circuit

In order to realize the inherent CCO and CVO, the LCT adopts the DDQ structure in this article. The coupled relationships of the LCT are shown in Fig. 6(a). The structure of the LCT is shown in Fig. 6(b). The DDQ coils could be used to remove cross-coupling between coils, which has been discussed in [29]. Therefore, the mutual inductance marked in

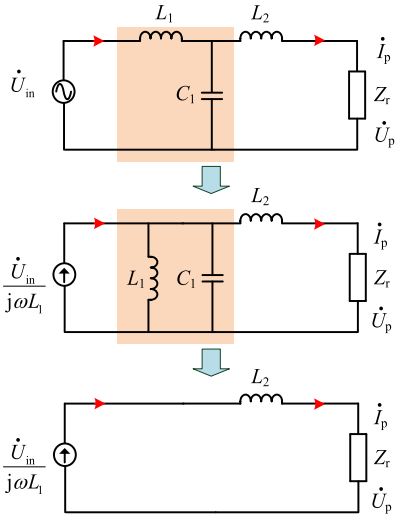

Fig. 7. Thevenin equivalent circuit of the *LCL* compensation network in the primary side.

red in Fig. 6(a) is nonexistent. The coupled relationships of the LCT shown in Fig. 6(a) could be expressed by the following equation:

$$\begin{bmatrix} j\omega L_{p1} & j\omega M_{12} & 0 & 0 \\ j\omega M_{12} & j\omega L_{s1} & 0 & 0 \\ 0 & 0 & j\omega L_{p2} & j\omega M_{34} \\ 0 & 0 & j\omega M_{34} & j\omega L_{s2} \end{bmatrix} \cdot \begin{bmatrix} i_1 \\ i_2 \\ i_3 \\ i_4 \end{bmatrix} = \begin{bmatrix} u_1 \\ u_2 \\ u_3 \\ u_4 \end{bmatrix}. \tag{13}$$

The primary *LCL* network is composed of the external elements L_1, C_1, and L_2. And the resonant relationship between them is shown in the following equation:

$$j\omega L_1 = \frac{1}{j\omega C_1} = j\omega L_2. \tag{14}$$

When the relationship in (14) is met, the equivalent circuit is shown in Fig. 7. Z_r is the reflected impedance of the parallel circuits. According to Thevenin's and Norton's theorems, when (14) is satisfied, the impedance of the *LC* parallel circuit is ∞. Consequently, the current in L_2 is constant and the current could be expressed by the following equation:

$$\dot{I}_p = \frac{\dot{U}_{in}}{j\omega L_1} \tag{15}$$

where the $\dot{U}_{in}$ is a sine source, and its amplitude is A_1.

Then, according to Fig. 3, the current $\dot{I}_P$ could be divided into two parts

$$\dot{I}_p = \dot{I}_{p1} + \dot{I}_{p2}. \tag{16}$$

Therefore, based on (13) and the structure of the circuit, the equivalent circuits after L_2 are shown in Fig. 8. The LCT is modeled as two T networks. And the circuit could be modeled as two two-port networks. The input voltages are both $\dot{U}_P$, and the input currents are $\dot{I}_{P1}$ and $\dot{I}_{P2}$, respectively. R_{ac1} and R_{ac2} are the equivalent ac resistance of the load. Based on the previous studies, the equivalent load of the battery could be regarded as a resistor. The resonant relationships of the

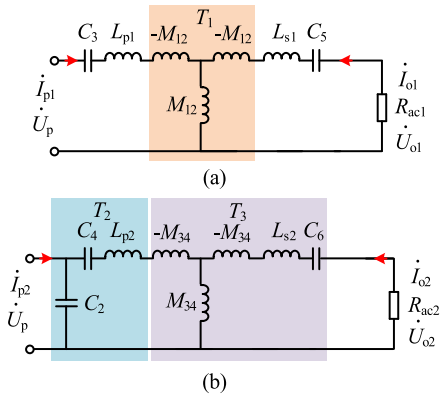

Fig. 8. Equivalent circuit of the proposed compensation network: (a) network I and (b) network II.

two networks in Fig. 8(a) and (b) are shown in the following equation:

$$\begin{cases} j\omega L_{p1} = \dfrac{1}{j\omega C_3} \\ j\omega L_{s1} = \dfrac{1}{j\omega C_5} \\ j\omega L_{p2} + \dfrac{1}{j\omega C_4} = \dfrac{1}{j\omega C_2}. \end{cases} \tag{17}$$

The two-port networks in Fig. 8 could be divided into several T networks. And their T-parameters matrices could be expressed by the following equation:

$$T_1 = \begin{bmatrix} 0 & -j\omega M_{12} \\ \dfrac{1}{j\omega M_{12}} & 0 \end{bmatrix} T_2 = \begin{bmatrix} 1 & \dfrac{-1}{j\omega C_2} \\ j\omega C_2 & 0 \end{bmatrix}$$
$$T_3 = \begin{bmatrix} 0 & -j\omega_s M_{34} \\ \dfrac{1}{j\omega_s M_{34}} & \dfrac{j\omega_s L_{S2} + \dfrac{1}{j\omega_s C_6}}{j\omega_s M_{34}} \end{bmatrix}. \tag{18}$$

Therefore, the two-port network in Fig. 8(a) could be expressed by

$$T = T_1 = \begin{bmatrix} 0 & -j\omega M_{12} \\ \dfrac{1}{j\omega M_{12}} & 0 \end{bmatrix}. \tag{19}$$

Similarly, the two-port network in Fig. 8(b) could be expressed by

$$T' = T_2 \cdot T_3 = \begin{bmatrix} \dfrac{1}{C_2 M_{34}\omega^2} & j\left(\dfrac{\omega L_{S2} - \dfrac{1}{\omega C_6}}{C_2 M_{34}\omega^2} - \omega M_{34}\right) \\ 0 & C_2 M\omega^2 \end{bmatrix}. \tag{20}$$

In order to realize the zero-phase-angle (ZPA) between the input voltage and input current in the two-port network in Fig. 8(b), the following equation should be satisfied according to [20]:

$$\frac{\omega L_{S2} - \frac{1}{\omega C_6}}{C_2 M_{34}\omega^2} - \omega M_{34} = 0. \tag{21}$$

Therefore, the value of C_6 could be expressed by the following equation:

$$C_6 = \frac{1}{\omega^2 L_{S2} - C_2 M_{34}^2 \omega^4}. \tag{22}$$

Then, the following equation should be satisfied:

$$\begin{cases} \left[\dot{U_p},\ \dot{I_{p1}}\right]^T = T\left[\dot{U_{o1}},\ -\dot{I_{o1}}\right]^T \\ \left[\dot{U_p},\ \dot{I_{p2}}\right]^T = T'\left[\dot{U_{o2}},\ -\dot{I_{o2}}\right]^T. \end{cases} \tag{23}$$

Then,

$$\begin{cases} \dot{I_{o1}} = \dot{U_p}\dfrac{1}{j\omega M_{12}} \\ \dot{U_{o1}} = \dot{I_{o1}} R_{ac1} \\ \dot{U_{o2}} = \dot{U_p}\omega^2 C_2 M_{34} \\ \dot{I_{o2}} = \dfrac{\dot{U_{o2}}}{R_{ac2}}. \end{cases} \tag{24}$$

The output voltage $\dot{U}_{o1}$ and $\dot{U}_{o2}$ could be expressed by $\dot{U}_p$ as shown in the following equation:

$$\begin{cases} \dot{U_{o1}} = \dot{U_p}\dfrac{R_{ac1}}{j\omega M_{12}} \\ \dot{U_{o2}} = \dot{U_p}\omega^2 C_2 M_{34}. \end{cases} \tag{25}$$

According to Fig. 8, the input impedances of two networks are Z_1 and Z_2. And Z_1 and Z_2 could be expressed by the following equation. The equivalent circuit is shown in Fig. 9

$$\begin{cases} Z_1 = \dfrac{\omega^2 M_{12}^2}{R_{ac1}} \\ Z_2 = \dfrac{R_{ac2}}{\omega^4 C_2^2 M_{34}^2}. \end{cases} \tag{26}$$

Due to the output of the two refilters being connected in parallel, the equivalent resistance of the battery could be expressed by

$$R_L = \frac{\pi^2}{8}\frac{R_{ac1} R_{ac2}}{R_{ac1} + R_{ac2}}. \tag{27}$$

At the beginning of charging, the equivalent resistance of the battery is small, and $Z_2 < Z_1$ should be satisfied. Therefore, $\dot{I}_{P2} > \dot{I}_{P1}$. The two networks are both operating. And the output is determined by the larger one between $\dot{U}_{o1}$ and $\dot{U}_{o2}$. According to (25), obviously, the output voltage is determined by $\dot{U}_{o2}$. However, the network in Fig. 8(a) does not stop working. This is because when the network in Fig. 8(a) stops working, the Z_1 will be zero, and the circuit will not work. Therefore, $U_{o1} = U_{o2}$. The value of R_{ac1} is fixed, and it could be expressed by

$$R_{ac1} = \omega^3 M_{12} C_2 M_{34}. \tag{28}$$

As the increasing of the equivalent resistance, the value of R_{ac1} will increase. When the R_{ac2} is equal to R_{ac1} as shown in the following equation, $Z_1 = Z_2$ will be satisfied according to (26). And $\dot{I}_{P1}$ is equal to $\dot{I}_{P2}$ at this time. As R_L continues to increase, the condition will be switching. $\dot{U}_{o1}$ will be larger than $\dot{U}_{o2}$, but the network in Fig. 8(b) will not block due to the R_L being still smaller than $8R_{ac1}/\pi^2$. Then, $U_{o1} = U_{o2}$ is still satisfied

$$R_{ac2} = \omega^3 M_{12} C_2 M_{34}. \tag{29}$$

During the above analysis, the value of R_{ac1} is always constant, and the output dc current I_{BAT} could be expressed by

$$\begin{aligned} I_{BAT} &= \frac{2}{\pi}\left(I_{o1peak} + I_{o2peak}\right) \\ &= \frac{2}{\pi}\left(\frac{I_{P1peak}\omega M_{12}}{R_{ac1}} + \frac{I_{P2peak}}{\omega^2 C_2 M_{34}}\right) = \frac{2I_{Ppeak}}{\pi\omega^2 C_2 M_{34}} \end{aligned} \tag{30}$$

where I_{o1peak}, I_{o2peak}, I_{p1peak}, I_{p2peak}, and I_{Ppeak} are amplitude values of corresponding alternating current. According to (15) and (30), the output dc current could be expressed by the following equation:

$$I_{BAT} = \frac{2A_1}{\pi\omega^3 C_2 L_1 M_{34}}. \tag{31}$$

A_1 is the amplitude value of $\dot{U}_{in}$. According to (31), the output current is load-independent, and the circuit could operate in the CCO mode. When the parameters of the LCT are determined, more design freedom of the output current can be achieved by adjusting the extra parameters L_1 and C_2.

As the R_L increases up to $8R_{ac1}/\pi^2$, R_{ac2} is nearly ∞, and network II will be blocked. $R_{ac1} = \pi^2 R_L/8$. Therefore, only network I shown in Fig. 8(a) is operating.

Then, according to (15) and (23), the output dc voltage could be expressed by the following equation:

$$U_{BAT} = \frac{\pi M_{12} A_1}{4L_1}. \tag{32}$$

Similarly, the output voltage is load-independent, and more design freedom of the output voltage can be achieved by adjusting the external inductance L_1.

In addition, the situation when the short circuit or open circuit happens on the load could be dealt with in the proposed circuit. When the load is short-circuited, R_{ac2} is zero and R_{ac1} still satisfies (28). The impedance Z_2 will be zero and $\dot{I}_{P1}$ will be zero. According to (30), the output current is still constant. And when the load is open circuit, the circuit will operate in the CVO mode. Therefore, when short circuit or open circuit happens on the load, the proposed circuit could operate normally. And when the secondary coil is moved accidentally, according to the relationship in (17), the impedance Z_1 will be zero, and the impedance Z_2 will be ∞. The constant current I_P will inject the coil L_{p1}, which will not damage the primary circuit. And the corresponding detection and protection circuits could be saved.

Based on the above analysis, the input impedance Z_{in} could be expressed by

$$Z_{in} = \frac{\omega^2 L_1^2 (Z_1 + Z_2)}{Z_1 Z_2}. \tag{33}$$

Based on the analysis in [20], Z_1 and Z_2 are both pure resistances. Therefore, the ZPA of the whole compensation network could be satisfied.

In this article, the value of A_1 is 158 V, M_{12} is 26.41 μH, M_{34} is 23.04 μH, and the U_{BAT} and I_{BAT} are set as 72 V

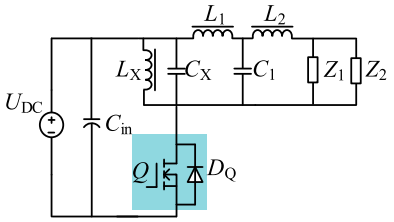

Fig. 9. Equivalent circuit of the proposed circuit.

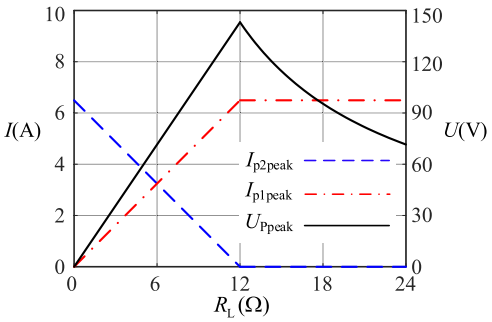

Fig. 10. Input current and input voltage of the parallel networks versus the equivalent load.

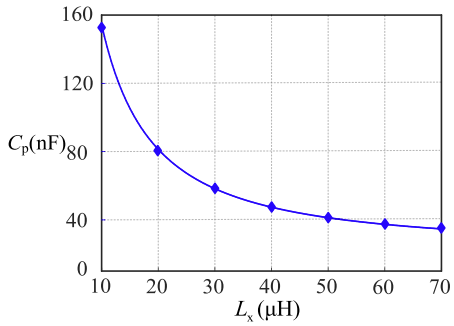

Fig. 11. Relationship between the C_p and L_X.

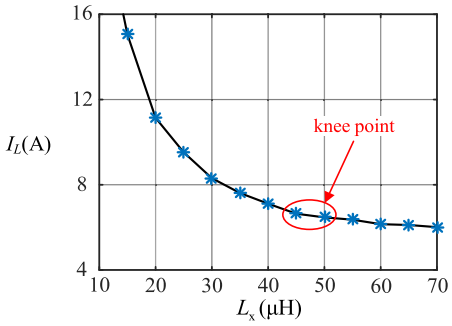

Fig. 12. Relationship between the I_L and L_X.

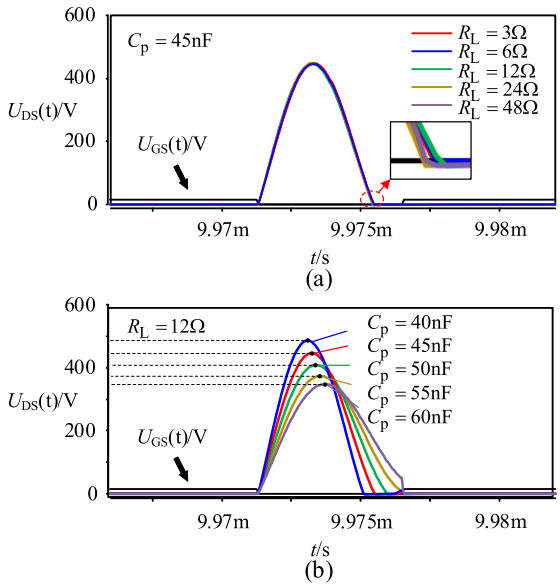

Fig. 13. ZVS condition versus the value of (a) Equivalent load RL. (b) C_p.

and 6 A, respectively. Therefore, the parameters I_{p1peak}, I_{p2peak}, and U_{Ppeak} versus the equivalent load R_L are shown in Fig. 10. As shown in Fig. 10, when the R_L is 6 Ω, I_{p1peak} equals I_{p2peak}. When the R_L is 12 Ω, the circuit in Fig. 8(b) will stop working. The tendency of the curve in Fig. 10 is consistent with the above analysis.

IV. Parameters Analysis of the Proposed Circuit

A. Value Selection of L_x and C_p

Based on the above analysis, the value of Z_{in} could be calculated. According to (3), keeping the value of the ω' is constant, the relationship between L_x and C_p is shown in Fig. 11. When $\omega\prime$ is constant, the value of A_1 could be kept constant. In this case, the current in L_x versus the inductance of L_x is shown in Fig. 12. As the improvement of L_x, the decreasing speed of the current I_L will be slower and slower. Therefore, the value of L_x should be chosen near the knee point of the curve in Fig. 12 to decrease the cost and power loss of the circuit. In this article, the value of L_x should be approximately 45 μH.

The value of C_p will influence the ZVS condition, and the ZVS margin D_{zvs} will influence the fundamental harmonic A_1. Before selecting the value of C_p, the influence of the load R_L should be analyzed. The ZVS condition versus the load R_L is shown in Fig. 13(a). However, the variation of the equivalent load has only a little influence on the ZVS condition. Therefore, the input voltage $u_{Cp}(t)$ could be considered constant. The relationship between the ZVS margin and the value of C_p is shown in Fig. 13(b). As shown in Fig. 13(b), the D_{ZVS} will increase when the value of C_p decreases. However, when the capacitance of C_p drops below 40 μF, the secondary vibration between the inductor and capacitor will occur, which causes the hard switching of the MOSFET. In addition, the D_{ZVS} will decrease when the value of C_p increases. The ZVS will fail to realize when the capacitance of C_p exceeds 55 nF.

When the inductance of L_X is kept constant, the variation of C_p will change the maximum value of $U_{DS}(t)$. In Section I, the maximum of $U_{DS}(t)$ is designed as 428.4 V. Therefore, the capacitance of C_p should be adjusted until the maximum of the $U_{DS}(t)$ up to approximately 428 V. The value of C_p could be obtained.

According to the above discussions, the design flowchart of key parameters is shown in Fig. 14. Based on the above discussion, the parameters of the proposed circuit are shown in Table II.

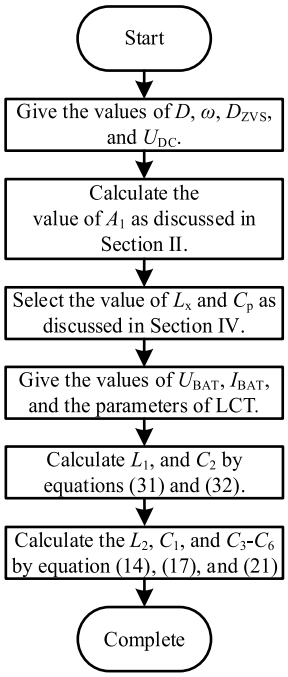

Fig. 14. Design flowchart of key parameters.

TABLE II
PARAMETERS OF THE PROPOSED CIRCUIT

Symbol	Definition	Value
L_X	Primary-side compensation inductor	45.2μH
C_p	Primary-side compensation capacitor	45nF
L_1	Primary-side compensation inductor	45.52μH
C_1	Primary-side compensation capacitor	77.02nF
L_2	Primary-side compensation inductor	45.52μH
C_2	Primary-side compensation capacitor	104.94nF
C_3	Primary-side compensation capacitor	58.26nF
C_4	Primary-side compensation capacitor	202.54nF
C_5	Secondary-side compensation capacitor	57.12nF
C_6	Secondary-side compensation capacitor	99.4nF
L_{P1}	The inductance of primary DD coil	60.18μH
L_{S1}	The inductance of secondary DD coil	61.38μH
M_{12}	Mutual inductance	26.41μH
L_{P2}	The inductance of primary unipolar coil	50.72μH
L_{S2}	The inductance of secondary unipolar coil	51.16μH
M_{34}	Mutual inductance	23.04μH
f_s	System operation frequency	85kHz
A_1	Calculated fundamental amplitude	158V
V_{BAT}	Output DC voltage	72V
I_{BAT}	Output DC current	6A
D	Duty cycle	0.55
D_{zvs}	ZVS margin	0.08

B. Influence of Z_{in} on the Circuit

In general, based on a different design of the compensation network, the equivalent load Z_{in} has three possible types, as shown in Fig. 15. As shown in Fig. 15(a), when the Z_{in} could be regarded as a series connection of resistance and capacitance, the equivalent circuit of C_p will change. In Fig. 15(a), the equivalent capacitance C_p' will resonate with L_X.

However, the value of C_p' is larger than C_p. Therefore, as discussed before, the ZVS margin will decrease, and the output of the inverter will be changed. During the operation of the circuit, the value of R_{in} and C_{eq} will change, and the

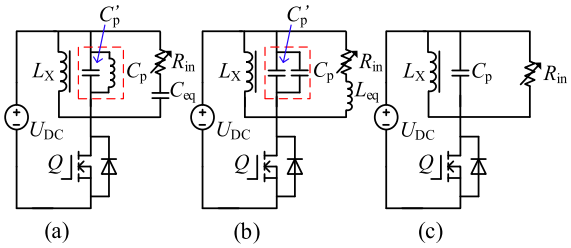

Fig. 15. Three possible equivalent circuits of the proposed topology when the Z_{in} is regarded as (a) C_{eq} and R_{in}. (b) L_{eq} and R_{in}. (c) R_{in}.

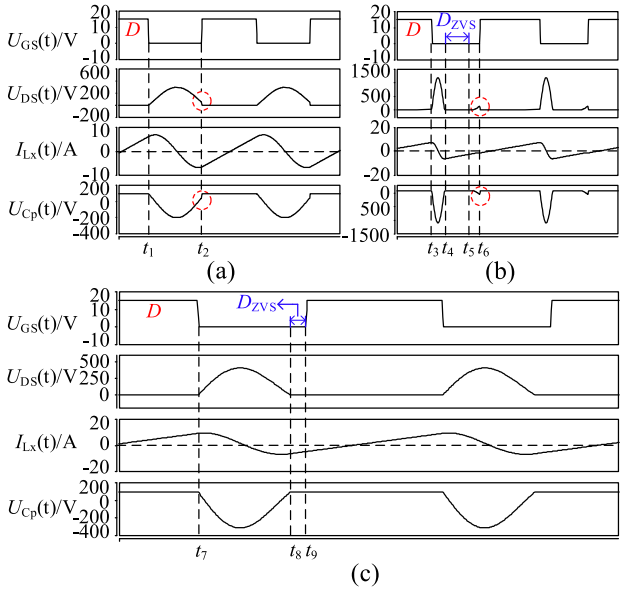

Fig. 16. Three corresponding operating states of Fig. 15 when the Z_{in} is regarded as (a) C_{eq} and R_{in}. (b) L_{eq} and R_{in}. (c) R_{in}.

value of C_p' will change simultaneously. Hard switching on the MOSFET may appear, as shown in Fig. 16(a). And the output of the inverter cannot be considered as constant. As shown in Fig. 15(b), the Z_{in} could be regarded as a series connection of resistance and inductance. The value of C_p' will be less than C_p. As the change of the equivalent load, the situation shown in Fig. 16(b) may appear. The ZVS will fail to realize, and the voltage stress of the MOSFET will be very high. When the Z_{in} is pure resistance as shown in Fig. 15(c), the operational condition of the circuit is shown in Fig. 16(c) when the value of C_p is appropriate. In this article, the Z_{in} is pure resistance, as discussed in Fig. 13(a), and the variation of the R_L has little effect on the operating state of the circuit. Therefore, the ZPA design of the compensation network is necessary for the proposed circuit.

In order to verify the realization of ZPA, the relationship between the input phase angle and the operating frequency is shown in Fig. 17. As shown in Fig. 17, no matter how the equivalent load changes, the proposed circuit could realize ZPA in CCO and CVO modes when the operating frequency is 85 kHz.

V. EXPERIMENTAL EVALUATION

In order to verify the performances of the proposed circuit, a single-switch WPT circuit with inherent CCO–CVO is built to provide 6-A load-independent current and 72-V

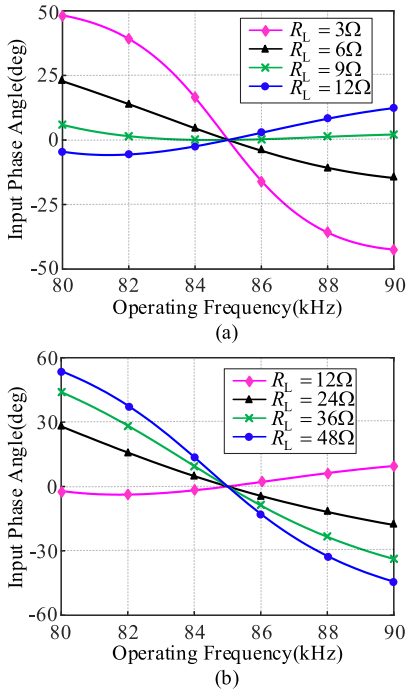

Fig. 17. Input phase angle versus the operating frequency in (a) CCO mode. (b) CVO mode.

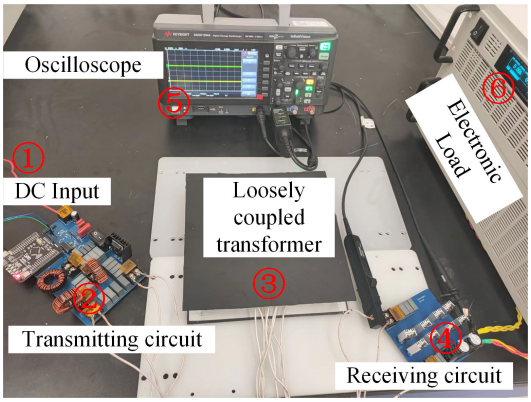

Fig. 18. Photograph of the proposed circuit.

load-independent voltage, as shown in Fig. 18. The input dc voltage is 96 V, and the operating frequency is 85 kHz. Both the primary and secondary coils consist of two groups, coaxial circular and DD coils with diameters of 20 cm, as shown in Fig. 19. The transmission distance is 3 cm. The experimental equipment consists of the dc input, single-switch *LC* inverter, LCT, secondary-side circuit, oscilloscope, and electronic load. The MOSFET is CGE1M120080 and the secondary-side rectifier diodes are eight MBR20150. The equivalent load of the battery is emulated by a dc electronic load. A control algorithm is implemented in an MCU STM32RCT6 for the experiments.

Fig. 20(a)–(d) shows the soft-switching waveform in CCO mode and CVO mode. The duty cycle is 55.44%. As shown in Fig. 20(a), when the R_L is 12 Ω, the measured amplitude of $U_{DS}(t)$ is 432 V, which is close to the calculated value 428.4 V. The D_{zvs} could be calculated as $\Delta X/T = 6.9\%$ from Fig. 20(a). This is because the duty cycle in the experiment is

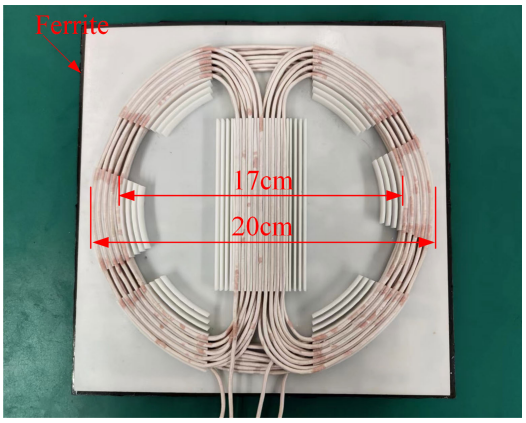

Fig. 19. Photograph of the LCT.

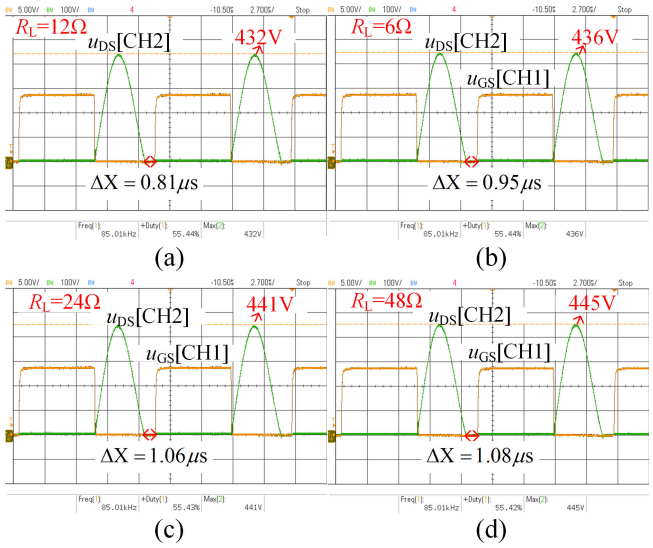

Fig. 20. Waveforms of ZVS in CCO mode and CVO mode: (a) waveform of ZVS when the R_L is 12 Ω; (b) waveform of ZVS when the R_L is 6 Ω; (c) waveform of ZVS when the R_L is 24 Ω; and (d) waveform of ZVS when the R_L is 48 Ω.

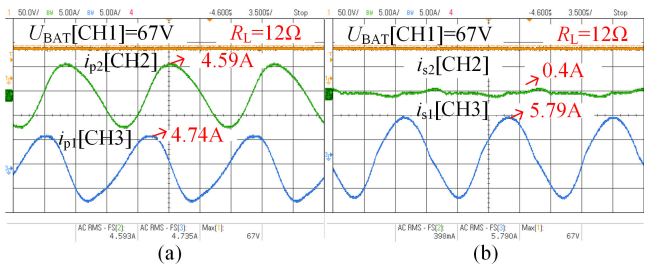

Fig. 21. Experimental waveforms of the current in the coils: (a) current in the primary coils when R_L is 12 Ω and (b) current in the secondary coils when R_L is 12 Ω.

larger than the design value. When the duty cycle is 55%, the D_{zvs} will be 7.3%, which is very close to the design value 8%.

In addition, as shown in Fig. 20(b) and (c), when the R_L is 6 (CCO) or 24 Ω (CVO), the D_{zvs} and the amplitude of $U_{DS}(t)$ will be increased, which is in accord with the discussion of Fig. 13(a).

Fig. 21(a) and (b) gives the waveforms of the currents in the primary and secondary coils with the output voltage as a

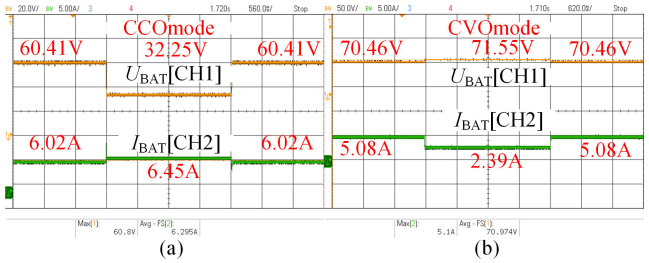

Fig. 22. Experimental waveforms of the output voltage U_{BAT} and output current I_{BAT}: (a) CCO mode with the load R_L changes from 10–5–10 Ω and (b) CVO mode with the load R_L changes from 15–30–15 Ω.

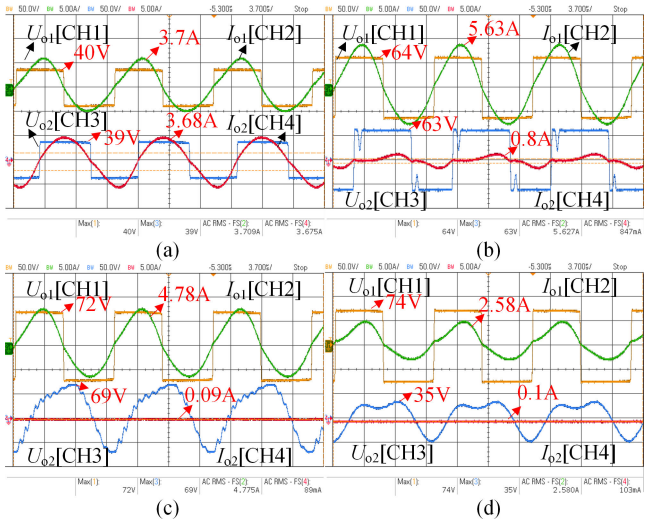

Fig. 23. Experimental waveforms of the ac output voltage and ac output current when the load R_L is: (a) 5 Ω; (b) 10 Ω; (c) 15 Ω; and (d) 30 Ω.

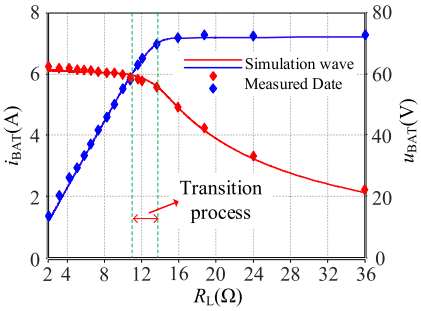

Fig. 24. Output parameters from experimental date and simulation waves versus the equivalent battery load.

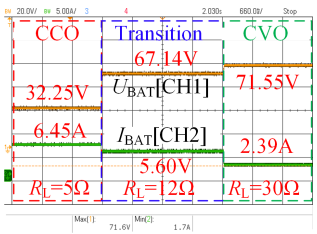

Fig. 25. Experimental waveforms of the output voltage U_{BAT} and output current I_{BAT}, when the load R_L changes from 5–12–30 Ω.

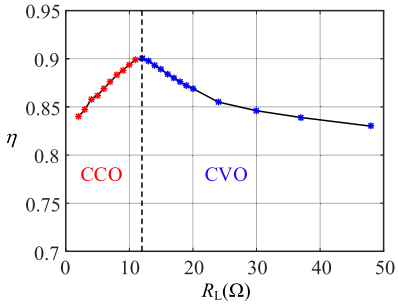

Fig. 26. Measured efficiency versus the equivalent battery load.

reference when the equivalent load is set as 12 Ω. As shown in Fig. 21(a), the rms values of currents in the L_{p1} and L_{p2} are 4.7 and 4.6 A, respectively. And the rms values of currents in L_{s1} and L_{s2} are 5.8 A and 398 mA, respectively, as shown in Fig. 21(b). As discussed in Section III, when the R_L is 12 Ω, the output of the circuit in Fig. 8(b) should be 0. The experimental waveform is consistent with the theoretical analysis.

Fig. 22(a) shows the waveforms of output voltage U_{BAT} and output current I_{BAT} in CCO mode. Obviously, when the load changes from 10 to 5 Ω, I_{BAT} will change from 6.02 to 6.45 A, and U_{BAT} will change from 60.41 to 32.25 V. The variation of output current is less than 8%, and the output current could be maintained at 6 A, which proves that the proposed single-switch WPT circuit has the characteristic of load-independent CCO. The characteristic of load-independent CVO could be verified in Fig. 22(b); when the load changed from 15 to 30 Ω, the output voltage could be maintained at approximately 72 V. And the corresponding ac waveforms are shown in Fig. 23. The current values marked in Fig. 23 are rms values. And the voltage values marked in Fig. 23 are maximum values.

The whole charging process is shown in Fig. 24, and the lines in Fig. 24 are simulation waveforms obtained by the SABER simulation software. And the rhombi is measured data obtained by the experiment. Different from the conventional CCO–CVO charging process, there is a transition process in the whole charging process, which is caused by the discontinuous current in the rectifier of the circuit in Fig. 8(b). The transition process could ensure the smooth switching between CCO mode and CVO mode. When the charging mode switching is realized by changing the frequency or the structure of the circuit, there is usually a shift in the output voltage and current, which may cause some impact on the battery.

The dynamic process of the charging mode change is shown in Fig. 25; when the load R_L changes from 5–12–30 Ω, the circuit will first change from CCO to the transition process, and then from transition process to CVO. And the whole process is automatic without any control.

The efficiency curve in the whole charging process is shown in Fig. 26. The efficiency is calculated by the dc input power and dc output power, and then processed by MATLAB. The maximum efficiency is 90.2%, and the maximum output power is about 374 W, when the equivalent load is approximately 12 Ω.

The power loss breakdown in Fig. 27 is calculated by the measured parameters when the output power is 374 W. During

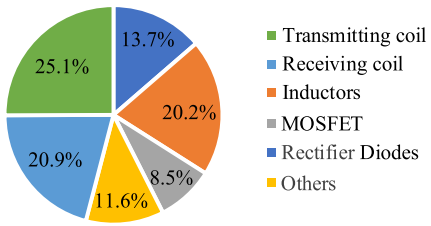

Fig. 27. Power loss breakdown among circuit components at R_L of 12 Ω.

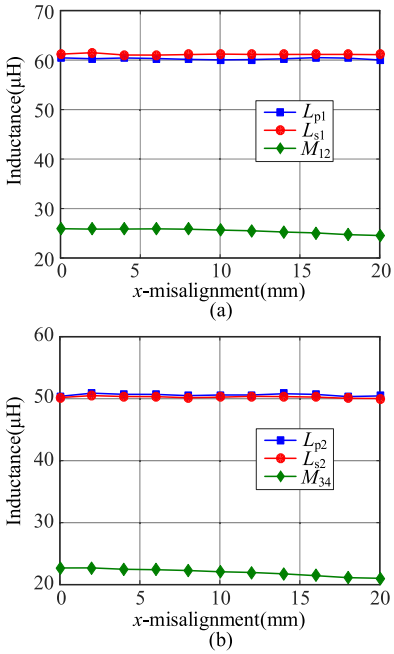

Fig. 28. Variation of the parameters of the LCT when the misalignment of coils occurs: (a) DD coils and (b) unipolar coils.

the experiment, the rms value of the current in each part can be measured by the current probe. And the equivalent series resistance (ESR) of passive devices used in this article could be measured by *LCR* meter. The power loss of MOSFET in this article is mainly the conducting resistance due to the waveform on the MOSFET. The conducting resistance R_{dson} of the MOSFEET in this article is 80 mΩ. And the rms value of the conducting current is 6.6 A. The power loss of the MOSFET is calculated as 3.48 W. The forward voltage drop of the rectifier diodes is 0.5 V. And the rms value of ON-state is 5.58 A. The power loss of the rectifier diodes is about 5.58 W. All the ac resistances of inductors used in this article measured by *LCR* meter are 100 mΩ. The rms values of the currents in L_1, L_2, and L_X are 4.7, 5.29, and 5.4 A, respectively. The power loss of the LCT is measured at 18.69 W. The power loss of the transmitting coils is higher due to there being currents in both the two transmitting coils, as shown in Fig. 21. Finally, the power loss of the others is calculated by the overall power loss and the power loss calculated before.

The DDQ coils adopted in this article have some misalignment tolerance in the x-axis, as shown in Fig. 6(b). The variation of the parameters of the LCT is shown in Fig. 28 when the misalignment of coils occurs. As shown in Fig. 28, the misalignment of the coils nearly does not cause

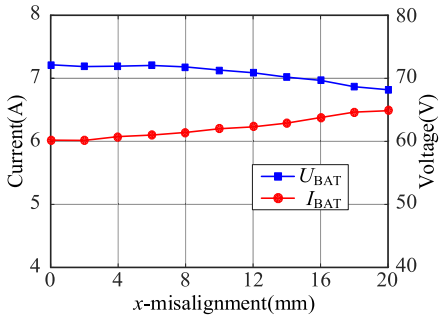

Fig. 29. Influence of the misalignment on the output.

the variation of the self-inductance of coils. However, the mutual inductances M_{12} and M_{34} will decrease a little when the misalignment of the coils occurs. In order to illustrate the influence of the misalignment on the output, the output current and output voltage when the misalignment of coils occurs are shown in Fig. 29. In this article, when the misalignment in the x-axis occurs, the output current in CCO mode and output voltage in CVO mode are still load-independent. Therefore, the values in Fig. 29 are the current values in CCO mode and voltage values in CVO mode measured in experiments. As shown in Fig. 29, as the increase of misalignment, the output current will increase and the output voltage will decrease. However, the variation of outputs is not obvious when the misalignment of coils occurs. In addition, in order to further improve the misalignment tolerance of the proposed circuit, the coil structure discussed in [30] and [31] could also be adopted in this article.

VI. Conclusion

This article proposes a single-switch WPT circuit with inherent CCO–CVO to realize load-independent output without the control circuit and wireless communication. The automatic transition from CCO to CVO could be realized. Different from the conventional full-bridge WPT converter, single-switch WPT circuit could avoid the shoot-through problem, which improves the reliability and decreases the cost of the system. The compensation design could enable primary-side protection of over current against the accidental removal of the secondary side. There is no inductor in the secondary circuit, which reduces the volume and weight of the secondary circuit. The transfer gain of the proposed circuit does not rely on the transformer parameters, which improves the design freedom of an LCT. A prototype with 6-A load-independent current and 72-V load-independent voltage is built. The ZVS could be realized in the whole charging process in this study. And the load-independent CCO and CVO have been verified in the experiment. The maximum efficiency of the proposed circuit could reach 90.2%. This design can be applied to various low-power or medium-power and low-cost wireless charging occasions.

References

[1] Y. Jang and M. M. Jovanovic, "A contactless electrical energy transmission system for portable-telephone battery chargers," *IEEE Trans. Ind. Electron.*, vol. 50, no. 3, pp. 520–527, Jun. 2003.

[2] J.-Q. Zhu, Y.-L. Ban, Y. Zhang, Z. Yan, R.-M. Xu, and C. C. Mi, "Three-coil wireless charging system for metal-cover smartphone applications," *IEEE Trans. Power Electron.*, vol. 35, no. 5, pp. 4847–4858, May 2020.

[3] Q. Li and Y. C. Liang, "An inductive power transfer system with a high-Q resonant tank for mobile device charging," *IEEE Trans. Power Electron.*, vol. 30, no. 11, pp. 6203–6212, Nov. 2015.

[4] Y. Li et al., "Analysis, design, and experimental verification of a mixed high-order compensations-based WPT system with constant current outputs for driving multistring LEDs," *IEEE Trans. Ind. Electron.*, vol. 67, no. 1, pp. 203–213, Jan. 2020.

[5] M. R. Basar, M. Y. Ahmad, J. Cho, and F. Ibrahim, "An improved wearable resonant wireless power transfer system for biomedical capsule endoscope," *IEEE Trans. Ind. Electron.*, vol. 65, no. 10, pp. 7772–7781, Oct. 2018.

[6] R. Sedehi et al., "A wireless power method for deeply implanted biomedical devices via capacitively coupled conductive power transfer," *IEEE Trans. Power Electron.*, vol. 36, no. 2, pp. 1870–1882, Feb. 2021.

[7] N. U. Hassan, S.-W. Hong, and B. Lee, "A robust multioutput self-regulated rectifier for wirelessly powered biomedical applications," *IEEE Trans. Ind. Electron.*, vol. 68, no. 6, pp. 5466–5472, Jun. 2021.

[8] D. Ahn and S. Hong, "Wireless power transmission with self-regulated output voltage for biomedical implant," *IEEE Trans. Ind. Electron.*, vol. 61, no. 5, pp. 2225–2235, May 2014.

[9] H. Li, Y. Yang, J. Chen, J. Xu, M. Liu, and Y. Wang, "A hybrid class-E topology with constant current and constant voltage output for light EVs wireless charging application," *IEEE Trans. Transport. Electrific.*, vol. 7, no. 4, pp. 2168–2180, Dec. 2021.

[10] K. Song et al., "Design of DD coil with high misalignment tolerance and low EMF emissions for wireless electric vehicle charging systems," *IEEE Trans. Power Electron.*, vol. 35, no. 9, pp. 9034–9045, Sep. 2020.

[11] L. Zhao, D. J. Thrimawithana, U. K. Madawala, P. Hu, and C. C. Mi, "A misalignment-tolerant series-hybrid wireless EV charging system with integrated magnetics," *IEEE Trans. Power Electron.*, vol. 34, no. 2, pp. 1276–1285, Feb. 2019.

[12] K. A. Cota, P. A. Gray, M. Pathmanathan, and P. W. Lehn, "An approach for selecting compensation capacitances in resonance-based EV wireless power transfer systems with switched capacitors," *IEEE Trans. Transport. Electrific.*, vol. 5, no. 4, pp. 1004–1014, Dec. 2019.

[13] D. Ahn, S. Kim, J. Moon, and I.-K. Cho, "Wireless power transfer with automatic feedback control of load resistance transformation," *IEEE Trans. Power Electron.*, vol. 31, no. 11, pp. 7876–7886, Nov. 2016.

[14] M. Huang, Y. Lu, and R. P. Martins, "A reconfigurable bidirectional wireless power transceiver for battery-to-battery wireless charging," *IEEE Trans. Power Electron.*, vol. 34, no. 8, pp. 7745–7753, Aug. 2019.

[15] X. Qu et al., "Wide design range of constant output current using double-sided LC compensation circuits for inductive-power-transfer applications," *IEEE Trans. Power Electron.*, vol. 34, no. 3, pp. 2364–2374, Mar. 2019.

[16] M. Fu, H. Yin, M. Liu, Y. Wang, and C. Ma, "A 6.78 MHz multiple-receiver wireless power transfer system with constant output voltage and optimum efficiency," *IEEE Trans. Power Electron.*, vol. 33, no. 6, pp. 5330–5340, Jun. 2018.

[17] Y. Li et al., "Reconfigurable intermediate resonant circuit based WPT system with load-independent constant output current and voltage for charging battery," *IEEE Trans. Power Electron.*, vol. 34, no. 3, pp. 1988–1992, Mar. 2019.

[18] D. Wang, X. Qu, Y. Yao, and P. Yang, "Hybrid inductive-power-transfer battery chargers for electric vehicle onboard charging with configurable charging profile," *IEEE Trans. Intell. Transp. Syst.*, vol. 22, no. 1, pp. 592–599, Jan. 2021.

[19] Y. Chen, H. Zhang, S.-J. Park, and D.-H. Kim, "A switching hybrid LCC-S compensation topology for constant current/voltage EV wireless charging," *IEEE Access*, vol. 7, pp. 133924–133935, 2019.

[20] X. Qu, H. Chu, S.-C. Wong, and C. K. Tse, "An IPT battery charger with near unity power factor and load-independent constant output combating design constraints of input voltage and transformer parameters," *IEEE Trans. Power Electron.*, vol. 34, no. 8, pp. 7719–7727, Aug. 2019.

[21] V.-B. Vu, D.-H. Tran, and W. Choi, "Implementation of the constant current and constant voltage charge of inductive power transfer systems with the double-sided LCC compensation topology for electric vehicle battery charge applications," *IEEE Trans. Power Electron.*, vol. 33, no. 9, pp. 7398–7410, Sep. 2018.

[22] J. Lu, G. Zhu, D. Lin, Y. Zhang, J. Jiang, and C. C. Mi, "Unified load-independent ZPA analysis and design in CC and CV modes of higher order resonant circuits for WPT systems," *IEEE Trans. Transport. Electrific.*, vol. 5, no. 4, pp. 977–987, Dec. 2019.

[23] Z. Huang, G. Wang, J. Yu, and X. Qu, "A novel clamp coil assisted IPT battery charger with inherent CC-to-CV transition capability," *IEEE Trans. Power Electron.*, vol. 36, no. 8, pp. 8607–8611, Aug. 2021.

[24] G. Li and H. Ma, "A hybrid IPT system with high-misalignment tolerance and inherent CC-CV output characteristics for EVs charging applications," *IEEE J. Emerg. Sel. Topics Power Electron.*, vol. 10, no. 3, pp. 3152–3160, Jun. 2022.

[25] Q. Zhang et al., "Research on input-parallel single-switch wireless power transfer system with constant-current and constant-voltage output," *IEEE Trans. Power Electron.*, vol. 37, no. 4, pp. 4817–4830, Apr. 2022.

[26] R. Yue, C. Wang, H. Li, and Y. Liu, "Constant-voltage and constant-current output using P-CLCL compensation circuit for single-switch inductive power transfer," *IEEE Trans. Power Electron.*, vol. 36, no. 5, pp. 5181–5190, May 2021.

[27] J. Wang, C. Wang, Z. Lu, Z. Guo, and S. Wang, "Single-switch wireless-power-transfer circuit with P-CLC compensation network used for battery charging," *IEEE Trans. Transport. Electrific.*, vol. 8, no. 3, pp. 4014–4026, Sep. 2022.

[28] G. Buja, M. Bertoluzzo, and K. N. Mude, "Design and experimentation of WPT charger for electric city car," *IEEE Trans. Ind. Electron.*, vol. 62, no. 12, pp. 7436–7447, Dec. 2015.

[29] Y. Li, T. Lin, R. Mai, L. Huang, and Z. He, "Compact double-sided decoupled coils-based WPT systems for high-power applications: Analysis, design, and experimental verification," *IEEE Trans. Transport. Electrific.*, vol. 4, no. 1, pp. 64–75, Mar. 2018.

[30] H. Li, M. Liu, L. Kong, and Y. Wang, "An independent dual-coil driving topology for wireless power transfer," *IEEE Trans. Power Electron.*, vol. 38, no. 2, pp. 1378–1383, Feb. 2023.

[31] Y. Chen et al., "A hybrid inductive power transfer system with misalignment tolerance using quadruple-D quadrature pads," *IEEE Trans. Power Electron.*, vol. 35, no. 6, pp. 6039–6049, Jun. 2020.

Jingyu Wang (Student Member, IEEE) was born in Taian, China, in 1996. He received the B.S. degree in electrical engineering and automation from the Hefei University of Technology, Hefei, China, in 2019, and the M.S. degree in electrical engineering from Qingdao University, Qingdao, China, in 2022. He is currently pursuing the Ph.D. degree with the Shien-Ming Wu School of Intelligent Engineering, South China University of Technology, Guangzhou, China.

His current research interests mainly include wireless power transfer.

Zhicong Huang (Member, IEEE) received the B.Eng. degree in electrical engineering and automation and the M.Eng. degree in mechanical and electronic engineering from the Huazhong University of Science and Technology, Wuhan, China, in 2010 and 2013, respectively, and the Ph.D. degree in power electronics from The Hong Kong Polytechnic University, Hong Kong, in 2018.

From January 2019 to February 2020, he was a Post-Doctoral Fellow under the UM Macao Talent Program with the State Key Laboratory of Analog and Mixed-Signal VLSI, University of Macau, Macao, China. He is currently an Associate Professor with the Shien-Ming Wu School of Intelligent Engineering, South China University of Technology, Guangzhou, China. His research interests include wireless power transfer, power electronics penetrated power system, electric vehicle, and intelligent engineering.

Dr. Huang received the Outstanding Reviewer Award from IEEE TRANSACTIONS ON POWER ELECTRONICS in 2021.